Title

Development of self-assembled multi-arm polyrotaxanes nanocarriers for systemic plasmid delivery in vivo

Authors

Ji, Ying
Liu, Xiangsheng
Huang, Max
et al.

Publication Date

2019-02-01

DOI

10.1016/j.biomaterials.2018.11.027

Peer reviewed

Published in final edited form as:

Biomaterials. 2019 February ; 192: 416–428. doi:10.1016/j.biomaterials.2018.11.027.

Development of self-assembled multi-arm polyrotaxanes nanocarriers for systemic plasmid delivery *in vivo*

Ying Ji[1], **Xiangsheng Liu**[1], **Max Huang**[1], **Jinhong Jiang**[2], **Yu-Pei Liao**[1], **Qi Liu**[2], **Chong Hyun Chang**[1], **Han Liao**[1], **Jianqin Lu**[1], **Xiang Wang**[2], **Melissa J. Spencer**[3], **Huan Meng**[*,1,2]

[1]Department of Medicine, Division of NanoMedicine, California NanoSystems Institute, University of California, Los Angeles, CA 90095, USA

[2]California NanoSystems Institute, University of California, Los Angeles, 90095 CA, USA.

[3]Molecular Biology Institute, University of California, Los Angeles, CA 90095, USA.

Abstract

Polyrotaxane (PRX) is a promising supramolecular carrier for gene delivery. Classic PRX exhibits a linear structure in which the amine-functionalized α-cyclodextrin (CD) is threaded along the entire polyethylene glycol (PEG) backbone. While promising *in vitro*, the absence of free PEG moieties after CD threading compromised the *in vivo* implementation, due to the unfavorable pharmacokinetics (PK) and biodistribution profile. Herein, we developed a multi-arm PRX nanocarrier platform, which has been designed for protective nucleic acid encapsulation, augmented biodistribution and PK, and suitable for intravenous (IV) administration. A key design was to introduce cationic CD rings onto a multi-arm PEG backbone in a spatially selective fashion. The optimal structural design was obtained through iterative rounds of experimentation to determine the appropriate type and density of cationic charge on CD ring, the degree of PEGylation, the size and structure of polymer backbone, *etc*. This allowed us to effectively deliver large size reporter and therapeutic plasmids in cancer mouse models. Post IV injection, we demonstrated that our multi-arm polymer design significantly enhanced circulatory half-life and PK profile compared to the linear PRX. We continued to use the multi-arm PRX to formulate a therapeutic plasmid encoding an immunomodulatory cytokine, IL-12. When tested in a colon cancer syngeneic mouse model with same background, the IL-12 plasmid was protected by the multi-arm PRX and delivered through the tail vein to the tumor site, leading to a significant tumor inhibition effect. Moreover, our delivery system was devoid of major systemic toxicity.

Keywords

gene delivery; systemic delivery; multi-arm polyrotaxane; interleukin-12; anticancer immunogenetherapy

[*]Corresponding author. Department of Medicine, Division of NanoMedicine, California NanoSystems Institute, University of California, Los Angeles, CA 90095, USA. menghuan.bj@gmail.com (H. Meng).

Competing interest

H.M. is the co-founder and equity holders in Westwood Biosciences, Inc.

1. Introduction

Polyrotaxane (PRX) is a mechanically interlocked molecule consisting of polymer backbone (strings) and macrocycles (rings), in which macrocycles are threaded onto a polymer, stabilized by bulky end groups [1]. When introducing positive charge on the rings, PRX becomes a promising carrier for the delivery of nucleic acids (*e.g.* plasmid and mRNA) due to a list of advantageous properties, such as efficient self-assembly, protective payload condensation, controllable nucleic acid loading and release, and versatile PRX functionalization [2–5]. Moreover, these materials are usually biocompatible due to the intrinsic safety of raw materials, such as polyethylene glycol (PEG) and cyclodextrin (CD) sugar rings that are used to construct PRXs [6]. While the *in vitro* transfection efficiency by the early-stage PRXs was competent with polyethyleneimine [6–11], they were rarely tested *in vivo*. This is partially because classic PRX has a linear axle; and the absence of free PEG moieties after CD threading leads to nano particulates subjected to rapid formation of protein corona and subsequent elimination by the reticuloendothelial system (RES) organs. The unfavorable pharmacokinetics (PK) and biodistribution profile are the major hurdles for the *in vivo* success. Moreover, there is a possibility that the colloidal instability of these low- or non-PEG protected PRX nanocarriers could lead to agglomeration in the circulation and therefore exclude the payload from the intended target site [12].

In this study, our aim is to develop an effective PRX platform for systemic delivery of nucleic acid *in vivo*. A key design feature was to introduce cationic CD rings onto a multi-arm PEG backbone in a spatially selective fashion. This resulted in functional PEG motif after CD threading and payload condensation, which served as a safeguard for plasmid delivery through intravenous (IV) administration (Figure 1A). To achieve the optimal effect *in vivo*, multi-arm PRX carrier was designed by iterative rounds of experimentation. We generated a series of multi-arm PRX analogues through tuning the key design features, such as cationic charge density, number of threaded CDs, level of available free PEG moieties, size of PEG backbones, *etc*. This allowed us to establish nano quantitative structure-activity relationship (QSAR) that was used to improve biodistribution, PK, and transfection efficiency using a tdTomato reporter plasmid and a therapeutic plasmid in cancer.

The optimized 4-arm PRX carrier was used for systemic delivery of an interleukin-12 (IL-12) encoding plasmid for immunogenetherapy in colon cancer. Although IL-12 is an important anti-tumor cytokine [13,14], the direct administration of recombinant IL-12 (rIL-12) was pharmacologically abandoned due to serious side effects, attributed to its unfavorable PK [13]. Among the alternatives is to use advanced delivery mechanisms (*e.g.* adenovirus [15], gene gun [16], electroporation [17] and nanoparticles [18]) for IL-12 plasmid (pIL-12) delivery, administrated intratumorally (IT) or intraperitoneally [17,19]. Very few IV option is available. Here, we have demonstrated that IV injected multi-arm PRX/pIL-12 nanocomplex exhibited favorable PK and abundant tumor biodistribution in mice, leading to efficacious and safe anti-tumor effect *in vivo*.

2. Results and Discussion

2.1 Development and optimization of 4-arm PRX gene delivery platform

We hypothesized that a multi-arm PRX with spatially selective CD threading can be used for effective plasmid delivery through systemic administration. This differs from the classic PRX design that requires CD threading along $-CH_2CH_2O-$ repeating units (EO units) in the entire linear PEG backbone [3]. While the positive linear PRX binds the plasmid *via* electrostatic interaction, the formation of none (or low) PEGylated but cationic nano particulates are generally inefficient for systemic application because of non-specific binding, short $t_{1/2}$ and unwanted RES uptake [20]. It is also found that IV-injected cationic nanoparticles typically ended up in the lung [11]. In this study, these challenges were overcame by the creative synthesis of a multi-arm PRX platform with carefully selected design features, which maintained the availability of functional PEG motif that was essential for systemic gene delivery *in vivo* (Figure 1).

For proof-of-principle, we used commercially available 4-arm PEG as a precursor to make PRXs. In general, the synthesis consists of the four steps, which are delineated in Figure 1B and Table S1. First, 4-arm PEG-tetra-amine was selectively end-capped with bulky groups (*i.e.*, fluorescein group) by controlling the feed ratio between the polymer and fluorescein-NHS (Step “I” in Figure 1B). Subsequently, the modified 4-arm PEG was added to a saturated aqueous solution of α-CD. For the fluorescein-NHS containing arms, the steric hindrance effect prevented α-CD from threading. For PEG arms ended with free amine, however, α-CD can be effectively threaded on, similar to the structure of linear PRX. We referred the former case as occupied PEG arm(s) that are free of α-CD molecules and therefore maintained the functional PEG motif (Step “II” in Figure 1B). This was followed by an amide coupling reaction to introduce Z-L-tyrosine to the amine terminals, which prevented the de-threading of α-CD (Step “III” in Figure 1B). Finally, amine functionalization was achieved by introducing N,N-dimethylethylenediamine (DMEA) to α-CD *via* carbonyldiimidazole (CDI) activation to generate cationic 4-arm PRX (Step “IV”, Figure 1B). Detailed synthesis procedures were described in the method section.

Optimization on cationic charge density.—Since multiple design characteristics were involved during the synthesis of 4-arm PRX, we decided to perform iterative optimization to obtain the optimal design features [21]. We began our optimization from positive charge density per α-CD because the cationic charge usually governed the self-assembly process and the delivery performances of non-viral carriers [22]. Accordingly, we prepared a library of 4-arm PRXs by adjusting the molar feed ratio of CDI to α-CD ranging from 5:1 to 30:1 (Step “IV” in Figure 1B). Other structural parameters, such as backbone size (*i.e.* 10 kDa) and the number of protective groups (*i.e.* 2 out of 4 arms are protected) were kept the same at this stage. The cationic charge density was determined *via* the integration of $-N(CH_3)_2$ (δg) from DMAE divided by the integration of C1(H) (δa) from α-CD in ^{1}H-NMR spectra (Figure 1C and S2A). This analysis demonstrated the successful synthesis of 3 PRXs with ~1, ~3 and ~6 amines *per* α-CD ring, respectively (Figure 1C).

To compare the *in vitro* effectiveness, we used the charge density controlled PRXs to deliver a tdTomato reporter plasmid (Addgene 30530, MW = 5.5 kbp) and tested on MC38 colon

adenocarcinoma cells. Briefly, PRXs were complexed with 1 μg tdTomato plasmid at various N/P ratios, ranging from 0.5:1 to 20:1. The heat map in Figure 1D provided a semi-quantitative display of the impact of charge density and N/P ratio on the transfection efficiency at 72 h. Compared to PRX with lower charge density, the best reporter expression was obtained by the PRX with 6 amines *per* α-CD at N/P ratio of 3:1. As expected, for PRXs with decreased charge density, the optimum N/P ratio shifted to higher values (Figure 1D). Comparing the transfection results at their optimum N/P, PRX with 6 amines *per* α-CD revealed significant increase over 3 amines *per* α-CD, while PRX with 1 amine *per* α-CD barely transfected MC38 cells. Since decreasing the charge density negatively affected the transfection efficiency, the following experimentation was performed at the fixed charge density, *i.e.* 6 amines per α-CD. Moreover, all these PRXs were devoid of cytotoxicity *in vitro*.

Optimization on the CD numbers.—The CD number *per* PRX can be adjusted by changing α-CD concentration during threading. Figure S2B demonstrated a representative case, *i.e.* 4-arm PRX with 2 free PEG arms, in which the CD number tunability ranged from 14~26 α-CDs *per* molecule. The tdTomato assay indicated that both transfection efficiency and plasmid loading were negatively impacted by the reduced number of α-CD (Figure S3A and Figure S3B). Consistent with previous report [7], saturated α-CD solution was used in the further experimentation.

Degree of free PEG arms.—By controlling the feed ratio of 4-arm PEG: NHS-fluorescein in the Step "I" in Figure 1B, we constructed 3 different PRXs with α-CD threading onto 1 out of 4 (1/4 ^{CD}), 2 out of 4 (2/4 ^{CD}) or 3 out of 4 arms (3/4 ^{CD}), respectively (Figure 2A and Figure S1). Synthesis success was confirmed by MALDI-TOF-MS (Figure 2B) and ^{1}H-NMR spectroscopy (Figure S1B). As demonstrated, the increase of average molecular weight was associated with increasing degree of end-capping. For example, the experimental molecular weight of 2/4^{CD} 4-arm PRX (10680 Da) was in close accordance with the theoretical molecular weight (10629 Da) (Figure 2B). A saturated α-CD solution was used to form different PRXs. In ^{1}H-NMR spectra, the integration of C1(H) peak (δa) from α-CD and $-CH_2CH_2O-$ peak (δf) from PEG were used to calculate the total number of α-CD *per* PRX polymer. As demonstrated in Figure 2C and Figure S2B, an average of 31 α-CDs *per* polymer was resulted from 3/4 ^{CD} PRX, while the total number of α-CDs decreased to 26 *per* 2/4 ^{CD} PRX and 12 *per* 1/4 ^{CD} PRX, due to the increased level of free PEG moieties (Figure 2C). While the degree of PEGylation on PRX/plasmid nano particulates requires additional assessment *in vivo*, it suffices to perform *in vitro* screening at this stage to exclude inefficient candidate in tissue culture (Figure 2D). We did not pursue 1/4 ^{CD} PRX because it exhibited the lowest transfection efficiency in MC38 cells. The result was in line with previous study, which suggested the excessive level of free PEG moieties could impede the access of polycation to plasmid DNA and reduced gene expression [23]. Since 2/4 ^{CD} and 3/4 ^{CD} PRXs behaved similarly *in vitro*, we focused on 2/4 ^{CD} PRX in order to achieve sufficient level of free PEG moieties, which was a favorable feature for IV administration.

Optimization on the size of polymer backbone.—Before animal testing, we also optimized the molecular weight of the 4-arm PEG backbone. In this case, additional 3 PRXs were constructed from 5 kDa, 10 kDa and 20 kDa 4-arm PEG polymers, and characterized by ^{1}H-NMR spectroscopy (Figure S2E and Figure S2D). The number of α-CDs *per* PRX polymer was positively correlated with the size of the 4-arm PEG backbone. 5 kDa 4-arm PRX required higher N/P ratio for tdTomato transfection compared to PRXs with 10 kDa or 20 kDa backbone (Figure S3C and Figure S3D), with > 4-fold reduction in transfection efficiency at optimum N/P ratio. The results suggested that the *in vitro* delivery performance of 4-arm PRX was molecular weight-dependent. This can be explained by the reduced level of plasmid condensation using low-molecular weight polycations. Similar phenomenon was also reported in other polycations such as poly(lysine) [24] and polyethyleneimine [25], *etc*.

In addition to MC38 cells, we also demonstrated abundant tdTomato expression in B16 melanoma cells (Figure S3E) treated by tdTomato plasmid delivered by the optimal 4-arm PRX. The results suggested that the 4-arm PRX platform could accommodate multiple cell types. The *in vitro* transfection effect was partially due to the effective particle uptake and lysosomal escape in MC38 cells (Figure S4). A separate MTS cytotoxicity assay demonstrated that the optimized 4-arm PRX was devoid of toxicity in MC38 cells at N/P ratio up to 100:1 (with the equivalent 4-arm PRX concentration up to 85 μg/mL) for 72 h (Figure S5).

Collectively, the combined use of PRX libraries and *in vitro* transfection study provided insights into our polymer design. Our *in vitro* optimized PRXs exhibited the following characteristics, *i.e*. 4-arm PEG backbone with a molecular weight of 10 kDa, 2 out 4 arms protected, ~26 CD rings *per* PRX molecule, and ~6 amines *per* CD ring. We are aware of other design features yet to be optimized, including the type of CD derivatives, the type of cationic groups, bulky end-caps with additional functionalities, *etc*. However, we decided to generate *in vivo* data at this point because the decision-making on these parameters may require *in vivo* data input as well as disease-specific considerations.

2.2 Improved pharmacokinetics (PK) and biodistribution in plasmid delivery by 4-arm PRX compared to linear PRX nanocarrier

The advent of *in vitro* optimized 4-arm PRX has prompted us to contemplate the *in vivo* application, including the demonstration of PRX therapeutic effect in a disease model, which is colon cancer in this case. Since IL-12 and tdTomato plasmids are similar in size (4.8 kbp vs 5.5 kbp), we used the optimized PRX to formulate pIL-12 with a hope to implement safe and efficacious immunogenetherapy. The self-assembly final product, referred as “pIL-12 4-arm PRX”, was visualized by AFM, and compared to free pIL-12 plasmid. The nanoparticles had a hydrodynamic size of 172 ± 8.7 nm (PDI=0.18) in water and 193 ± 6.2 nm (PDI = 0.17) in cell culture media (DMEM supplemented with 10% FBS). The average zeta potential values were 15.3 ±3.2 mV in water, and −3.95 ± 1.9 mV in DMEM plus 10% FBS. Other physicochemical characteristics, including N/P ratio, hydrodynamic size, endotoxin level and sterility, were shown in the table in Figure 3A.

PK and biodistribution studies were performed in C57BL/6 mice using 4-arm PRX. To quantify plasmid concentration in the blood, plasmid was covalently labeled by Cy3

fluorophore. Animals were IV injected with Cy3-labeled plasmid laden 4-arm PRX at a dose of 5 mg plasmid/kg. The control was the nano particulates formed by linear PRX complexed with the same amount of plasmid, which exhibited similar level of gene packaging capabilities (Figure S6), *in vitro* transfection efficiency (Figure S7) and primary particle size (189 ± 7.4 nm, PDI = 0.22). Plasma was collected at the indicated time points (0.083, 1, 2, 4, 8 and 24 h). The plasmid concentration in each sample was calculated based on the fluorescence intensity, and expressed as total %ID/mL (total injection dose *per* mL) (Figure 3B). The 1st measurement at 0.083 h represented C_{max}. The PK parameters of each formulation were assessed using PKSolver software [26]. In the linear PRX group, the linear PRX exhibited a circulatory $t_{1/2}$ of 0.08 h. This clearly contrasted with 4-arm PRX carrier, which exhibited a $t_{1/2}$ value of 5.8 h. The $AUC_{(24h)}$ values for 4-arm and linear PRXs were 73.5 %ID/mL•h and 8.8 %ID/mL•h, respectively.

To further corroborate the contrast PK profiles, we incubated plasmid laden 4-arm PRX or linear PRX nanoparticles (1 μg plasmid/μL) with 10 μg/μL IgG, a representative opsonin protein during opsonization, according to a published protocol [27]. Compared to linear PRX, native gel electrophoresis revealed significantly reduced IgG binding to 4-arm PRX nanoparticles (*i.e.* 27% protein bound particle) (Figure 3B, right panel). In contrast, we found a pronounced IgG/linear PRX interaction (*i.e.* 98% protein bound particle), which suggested a strong opsonization effect in the blood post IV injection [28]. The original gel image was shown in Figure S8. Without resorting to a comprehensive proteomic approach to quantitatively determine the protein corona composition in the different PRX carriers, we speculate that the reduced interaction between 4-arm PRX particle and opsonin protein contributed to its prolonged circulatory $t_{1/2}$ and enhanced PK profile *in vivo*.

It is generally believed that IV-injected nanoparticles tend to accumulate in solid tumor partially due to the enlarged vasculature fenestration at tumor site [29]. We continued to ask if the pIL12 4-arm PRX nanocomplex has adequate tumor access, such as a MC38 colon cancer site. Subsequently, C57BL/6 mice bearing subcutaneous MC38 tumor received IV injection of Cy3-labeled plasmid delivered by 4-arm PRX (5 mg plasmid/kg). Identical amount of plasmid delivered by linear PRX carrier was used as control. To determine the biodistribution, *ex vivo* imaging of the tumor and major organs was performed 24 h post injection (Figure 3C). The plasmid fluorescent signal intensities in tumors and other organs were quantified by IVIS software and normalized to control. The majority of plasmid delivered by linear PRX was entrapped in lung, the most typical off-target organ for cationic gene carrier [11]. The linear PRX carrier barely distributed in tumor, presumably due to non-specific binding and rapid clearance of opsonin-attached nanocarrier (Figure 3C). However, when delivered by 4-arm PRX, minimized distribution in lung was observed (similar to control mice). Abundant plasmid uptake biodistributed to the tumor site (Figure 3C). The liver was still a major site of plasmid distribution, a phenomena commonly observed for IV injected nanoparticles subjected to sequestration by Kupffer cells [30]. Hardly any plasmid was detected in the heart, spleen or kidney. A semi-quantitative display of Cy3 fluorescence intensity was shown (Figure 3C, right panel). To interpret the intratumoral distribution of Cy3-labeled plasmid, the tumor blood vessels were stained with CD31 immunofluorescence (Figure 3D). We demonstrated higher pIL-12 plasmid abundance at the tumor site in the case of 4-arm PRX. The CD31 staining suggested the plasmid delivered by 4-arm-PRX traveled

from blood vessels and accessed the tumor tissue. Perinuclear distribution of plasmid was confirmed. Moreover, we realized that particle distribution in the MC38 tumor was heterogeneous, similar to our previous discovery in pancreatic cancer and drug resistant breast cancer models [31,32]. While we have the options to use TGFβ inhibitor delivery nanocarrier [33] or a transcytosis inducing iRGD peptide [34] to improve particle intratumoral distribution, the immunomodulatory effect of IL-12 in the tumor microenvironment does not require the homogenous particle uptake in each cancer cells.

We also performed a separate *in vivo* reporter transfection study with IV injected tdTomato plasmid (5 mg plasmid/kg) delivered by 4-arm or linear PRX carriers in the MC38 tumor model. Western blot identification of protein expression from tumor extracts was performed 7 days post injection (Figure S9). As expected, hardly any tdTomato expression was detected in MC38 tumors receiving linear PRX. However, tdTomato signals were clearly identified in 4-arm PRX treated tumor, which confirmed the feasibility of systemic delivery of plasmid by 4-arm PRX.

Collectively, careful tuning of the free PEG moieties on 4-arm PRX effectively enhanced the PK profile and distribution, and did not significantly compromise gene packaging properties or transfection efficiency *in vivo*. Given this background, we continued to use this optimized 4-arm PRX for therapeutic IL-12 plasmid delivery in the same syngeneic MC38 colon cancer model.

2.3 Systemic delivery of interleukinin-12 plasmid by 4-arm PRX led to efficacious anti-tumor effect through concurrent activation of innate and adaptive immunity

IL-12 plasmid (pIL-12) encodes a potent immune-stimulatory cytokine that bridges the innate and adaptive immunity against tumor [13]. IL-12 targets natural killer (NK) cells and T lymphocytes, effectively stimulating the secretion of IFN-γ (a cytokine coordinating anticancer defense) [35]. Moreover, the potency of IL-12 was demonstrated in various solid tumor models for both immunogenic (*e.g.* CT26 colon cancer [36], RENCA renal cancer [37]) and poorly immunogenic tumor models (*e.g.* LLC lung cancer [38], B16 melanoma [39]) in mice. While there is high level of interest in using IL-12 for solid tumor treatment, practical use of IL-12 as a cancer therapy requires novel delivery mechanism. Recombinant IL-12 (rIL-12) protein was abandoned in the clinical trials because of unfavorable PK and serious side effects, such as fatal pulmonary, hepatic, intestinal and hematopoietic toxicities [40] post IP [41] and IV [42] administration in patients. We asked if our pIL-12 4-arm PRX delivery system can be used to implement IL-12 therapy effectively and safely.

The 1st set of animal experiment was a short-term study, in which pIL-12 laden 4-arm PRX was IV injected once (5 mg plasmid/kg) into MC38 tumor mice (Figure 4A). 3 or 7 days post injection, tumors and major organs were harvested for ELISA detection of IL-12 (p70). At both time points, significantly enhanced IL-12 production was observed in 4-arm PRX group compared to saline control at tumor site (Figure 4A). In most normal organs, such as spleen, lung, kidney and heart where rIL-12 leads to major toxicity [43], no significantly elevated IL-12 was detected (Figure S10). Importantly, IV pIL-12 PRX did not generate detectable IL-12 level in serum, which is crucial in reducing systemic off-target toxicity [40]. With a view to elucidate any nonspecific IL-12 stimulation (presumably related to the

general immunogenicity of bacteria-derived plasmid) [44], tumor mice receiving control plasmid laden 4-arm PRX (pC 4-arm PRX) were used as an additional control. Our data demonstrated that no significant secretion of IL-12 was found in tumors receiving IV pC laden 4-arm PRX. This finding is in agreement with literature [45]. Moreover, the time-dependency of IL-12 expression at the tumor site provided the rationale for planning the injection regimen in the following efficacy study.

For the anti-tumor efficacy study, we subcutaneously implanted luciferase-expressing MC38-luc cells to C57BL/6 mice. The mice received IV injections of 5 mg plasmid/kg twice per week, 5 injections in total (Figure 4B). Control mice received IV injection with saline or pC laden 4-arm PRX (as non-functional control). Tumor growth was monitored *in situ* by IVIS bioluminescence imaging (Figure 4B), followed by euthanasia of animals on day 21. Quantitative expression of tumor growth by IVIS (the intensity of tumor signals normalized to day 1), demonstrated significantly slower tumor growth when treated by IV injection of pIL-12 laden 4-arm PRX, compared to controls.

Shown in the schematic Figure 4C, as a potent inducer of anti-tumor immunity, IL-12 directly augments the proliferation and cytolytic potential of NK cells and promotes the development of $CD8^+$ T cells in tumor microenvironment, including colon cancer [46,47]. In addition, the anti-angiogenesis activity by IL-12 contributes pivotally to the tumoricidal efficacy [14]. To dissect the immunomodulatory effect, the tumor tissues in Fig. 4A were used for IHC and multi-parameter flow cytometry analysis [48]. IHC staining for CD8, NK1.1 and IFN-γ^+ showed that pIL-12 laden 4-arm PRX resulted in significantly enhanced recruitment of $CD8^+$ T cells along with NK cells (Figure 4D). These findings were corroborated by flow cytometry (Figure 4D and Figure S12), suggesting that pIL-12 4-arm PRX enhanced the $CD45^+CD3^+CD8^+$ TILs populations (by 1.8-fold) and $CD45^+NK1.1^+$ populations (by 4-fold) compared to saline or pC controls. As a central effector in IL-12-mediated anti-tumor immunity, significantly increased IFN-γ release was revealed by IHC staining of pIL-12 4-arm PRX treated tumor section (Figure 4D). Phenotypic identification of $CD45^+CD8^+$ IFN-γ^+ and $CD45^+NK1.1^+$IFN-γ^+ population suggested that the recruited NK cells and $CD8^+$ T cells were the sources for IFN-γ^+ production. Furthermore, immunofluorescence staining of $CD31^+$ blood vessels (Figure 4E) demonstrated distinct anti-angiogenesis effect in tumor sections treated by pIL-12 laden 4-arm PRX. Our nanoparticle led to ~75% reduced blood vessel density compared to controls.

2.4 pIL-12 laden 4-arm PRX improved toxicity profiles in mice compared to rIL-12

The major reason for the rIL12 failure is its safety issue [13]. Rapid buildup of rIL12 leads to significant systemic toxicity, including a severe impact on hepatic serum enzymes, leukopenia, pulmonary edema and mononuclear cell and macrophage infiltrates in multiple tissues [40]. The possibility of reducing IL-12 toxicity by plasmid delivery is one of the major objectives of this study. In order to compare with PRX mediated plasmid delivery, we included a control using mouse rIL-12 protein at 100 μg/kg, a therapeutic dose in the literature [37] that exhibited similar antitumor effect to our pIL-12 4-arm PRX in the MC38 tumor bearing mice (Figure S11). In a separate experiment, we performed IV injections following exactly the same treatment regimen described in Figure 4B in normal C57BL/6

mice. We used normal mice because the large tumor burden may lead to complexity for the toxicity data interpretation. The repetitive IV administration of pIL-12 laden PRX did not elicit adverse effects in most of parameters from blood biochemistry measurement, such as liver function enzymes (*e.g.* AST, ALT, ALP), kidney panel (BUN and creatinine) at both day 7 and day 21 (Figure 5A). Transit and moderate decrease of blood immune cells were observed in mice receiving pIL-12 4-arm PRX on day 7; however, these changes were transit and reversible at day 21 without the need of medication. Animals treated with rIL-12 exhibited severe and across the board abnormalities to multiple organs in the blood chemistry analysis, similar to the life-threading side effects in patients [49]. Moreover, rIL-12-induced adverse changes were persistent, up to 21 days post treatment. Histological assessment demonstrated that animals receiving rIL-12 showed sign of pulmonary toxicities, such as pulmonary edema and interstitial thickening in H&E staining of lung section (Figure 5B). In contrast, no damage was seen in the lungs of animals treated with saline and pIL-12 laden PRX. In the rIL-12 group, histological assessment of kidney tissues showed glomerular swelling and edema of Bowman's space in the glomeruli of the kidneys (Figure 5B). Liver histology of rIL-12 treatment revealed severe mononuclear cell infiltration (Figure 5B). Attenuated mononuclear cell infiltration was observed in pIL-12 PRX treated group, which failed to lead to liver enzyme abnormality (Figure 5A). This marked the reduced inflammation and damage in liver tissues. No lesions or abnormalities were observed in other organs such as heart and spleen, as demonstrated in Figure S13.

For IL-12, there is continuous interest and critical need to improve PK and safety, which is the key for the practical implementation of IL-12 cancer immunotherapy. Other strategies have emerged including developing tumor-targeting IL-12 derivatives (NHS-IL-12) [50] and IL-12 gene therapeutics [51]. GEN-1 [52] formulated with IL-12 plasmid and PEG-PEI-cholesterol lipopolymer, is designed for IP administration in ovarian cancer. Unlike ovarian cancer that primarily disseminates within the peritoneal cavity with massive ascites [53], colon cancer is a deep-seated solid tumor that metastasizes hematogenously and lymphatically to lung and liver [54, 55]. While local injection of IL-12 might lead to systemic anti-cancer immunity, safe and effective IV-injectable formulation is still the preferred route for pIL-12 delivery from the tumor targeting perspective [56].

While our current formulation (that relies on passive targeting principle to biodistribute at colon cancer site) has led to promising data, we can also include tumor targeting ligand such as targeting peptide [34]. However, we do consider the design complexity and the cost increase of each component in terms of clinical application. Moreover, preclinical and clinical data have suggested the benefit of IL-12 combination therapy because repeated IL-12 dosing may activate various immunosuppressive mechanisms [57]. Thus, it is also necessary to consider pIL-12 PRX in combination with treatments such as other cytokines (*e.g.* IL-2) [58], neoadjuvant chemotherapeutic agents (*e.g.* oxaliplatin, doxorubicin and paclitaxel) [10] and checkpoint inhibitors (*e.g.* anti-PD-1, anti-PD-L1, anti-CTL4 and IDO inhibitors) [59].

The multifunctional properties of multi-arm PRX can be further tuned to accommodate different clinical needs for nucleic acid delivery. In Scheme 1, we included a list of structural design features and their possible outcomes. Fine-tuning of cationic entities and their spatial

arrangement, as well as other components along PRX structure (*e.g.* targeting), can make this delivery platform available for multiple APIs, including large plasmid (*e.g.*, CRISPR/Cas9 plasmid for gene editing). It is also necessary to point out the recent advance for PRX mediated delivery *in vivo*, *i.e.* zwitterionic poly(carboxybetaine) grafted PRX for paclitaxel delivery [60] poly(ethylenimine)-grafted PRX functionalized with folate for tumor targeting delivery [61] and β-cyclodextrin-based polyrotaxane for cancer theranostics [62]. This valuable information could be complementary to our discovery to enrich the growing list of the design features of PRX.

3. Conclusions

To conclude, we have established a multi-functional multi-arm PRX platform that is suitable for systemic nucleic acid delivery. Our comprehensive biodistribution and PK analyses demonstrated that the spatially selective design in multi-arm PRX polymer maintained appropriate degree of PEGylation, which played a key role for the improved PK and bioavailability. When delivering a pIL-12 plasmid to a colon tumor site, we have demonstrated an efficacious and safe immunogene therapy at intact animal level.

4. Materials and Methods

4.1 Materials

α-Cyclodextrin, triethylamine (TEA), Z-L-tyrosine, Benzotriazol-1-yl-oxy-tris(dimethylamino) phosphonium hexafluorophosphate (BOP), 1-hydroxybenzotriazole (HOBt,) N,N-diisopropylethylamine (DIEA), 1,1′-carbonyldiimidazole (CDI), N,N-dimethylethylenediamine (DMAE), dimethylformamide (DMF), dimethyl sulfoxide (DMSO) were purchased from Sigma Aldrich. Four-arm PEG tetra-amine hydrochloride salt with different molecular weight (5 kDa, 10 kDa or 20 kDa) and linear PEG-diamine hydrochloride salt (3.5 kDa) were purchased from Jen Kem Technology. NHS-fluorescein and Snakeskin dialysis tubing (MWCO= 3.5 kDa or 10 kDa) were purchased from Thermo Fisher. Plasmid pUNO1-mIL12 (p40p35) (4.8 kbp, designated as pIL-12) encoding mouse IL-12 p70, was provided by InvivoGen. Plasmid encoding tdTomato reporter protein was provided by Addgene (Addgene plasmid 30530). Matrigel™ matrix basement membrane was purchased from BD Bioscience, USA. Centrifugal filter units (MWCO= 3 kDa, 10 kDa, 100 kDa) were purchased from EMD Millipore.

4.2 Synthesis of 4-arm PRX analogues

4-arm-PEG backbone with end-caps.—4-arm PEG tetra-amine hydrochloride salt 10 kDa (103 mg) was dissolved in DMF (5 mL) with TEA (6 mg) before NHS-fluorecein was added and stirred at room temperature for 24 h. The amount of NHS-fluorecein was manipulated to achieve different number of fluorescein end-caps, i.e., 4.7 mg NHS-fluorecein for 1-occupied 4-arm PEG amine (4-arm PEG: NHS-fluorescein = 1:1 molar ratio), 9.5 mg NHS-fluorecein for 2-occupied 4-arm PEG amine (4-arm PEG: NHS-fluorescein = 1:2 molar ratio) and 14.2 mg NHS-fluorecein for 3-occupied 4-arm PEG amine (4-arm PEG: NHS-fluorescein = 1:3 molar ratio), respectively. The resulting solution was precipitated in cold diethyl ether, dissolved in DI water and purified by repeated

washing with DI water in centrifugal filter units (MWCO=3 kDa), and lyophilized (Labconco FreeZone). To detect the average molecular weight after modification, 4-arm PEG amine compounds with different number of fluorescein end-caps were dissolved in THF/H_2 O (1:1, v/v) at a concentration of 10 mg/mL for MALDI-TOF (Bruker Ultraflex). Fluorescein occupied 4-arm PEG amine compounds were dissolved in deuterated water for ^{1}H-NMR spectroscopy.

4-arm Polypseudorotaxane.—Fluorescein occupied 4-arm PEG amine (100 mg) was added to a saturated solution of α-CDs (1.01 g in 7 mL of DI water) and stirred at room temperature for 24 h, resulting in supramolecular polypseudorotaxane formed from α-CDs threading onto 4-arm PEG backbone. The precipitate was collected via centrifugation at 3,000 rcf for 10 min and lyophilized to obtain 4-arm polypseudorotaxane as yellow powder. To prepare 4-arm polypseudorotaxane with reduced numbers of α-CDs, unsaturated solution of α-CDs (0.35 g in 7 mL of DI water; 0.70 g in 7 mL of DI water) was used, and resulted in 14 α-CDs per 2/4^{CD} PRX or 19 α-CDs per 2/4^{CD} PRX, respectively.

4-arm Polyrotaxane.—To prevent the de-threading of α-CDs, bulky end caps (Z-tyrosine) were further introduced to 4-arm polypseudorotaxane. An example was given here for 2/4^{CD} 4-arm polypseudorotaxane preparation. Z-L-tyrosine-OH (126 mg), HOBt (54 mg), BOP (177 mg) and DIEA (69 μL) were dissolved in 2.5 mL anhydrous DMF. 370 mg polypseudorotaxane was then added and the reaction was stirred at room temperature for 24 h. The mixture was precipitated in 50 mL diethyl ether, and sequentially washed by acetone (50 mL), methanol (50 mL) and DI water (15 mL). Each washing steps were 2 h at room temperature under constant stirring and the precipitate was collected via centrifugation at 3,000 rcf for 10 min. After the last washing step, the 4-arm polyrotaxane was lyophilized. ^{1}H-NMR was performed in DMSO-d_6 to characterize the product.

4-arm Polyrotaxane-DMAE.—An example was given here for the synthesis of 2/4^{CD} 4-arm PRX with 6 amines per CD. Z-L-Tyrosine capped 2/4^{CD} 4-arm polyrotaxane (100 mg) was dissolved in dry DMSO (2 mL). CDI (364 mg, 30 molar excessive to α-CDs) was added and the reaction was stirred for 3 h under nitrogen atmosphere. DMAE (1 mL) was then added dropwise to the solution, and the reaction was further stirred overnight at room temperature. The resulting mixture was precipitated in diethyl ether, and washed sequentially by acetone (50 mL) and methanol (50 mL). Each washing steps were 2 h at room temperature under constant stirring and the precipitate was collected via centrifugation at 3,000 rcf for 10 min. The precipitate was redissolved in DI water and dialyzed against DI water for 72 h (MWCO = 3 kDa). The final product of 4-arm PRX was lyophilized as yellow powder. The density of amine functionalization on α-CD was manipulated via tuning the feed ratio between CDI and α-CDs in 4-arm polyrotaxane. CDI at 5 molar excessive to α-CDs resulted in 4-arm PRX with 1 amine group per CD, and CDI at 20 molar excessive to α-CDs resulted in 3 amine groups per CD, respectively. The purified 4-arm PRX was lyophilized and ^{1}H-NMR characterization was performed in deuterated water to characterize the product. In addition, 2/4^{CD} 4-arm polyrotaxane-DMAE with 5 kDa or 20 kDa 4-arm PEG backbone were synthesized, following the same procedures and molar ratio between reactants for 2/4^{CD} 4-arm polyrotaxane-DMAE (6 amines per α-CD) with 10 kDa backbone.

4.3 Synthesis of linear PRX

The synthesis of linear PRX was performed as previously reported [3]. 100 mg of linear PEG-diamine hydrochloride salt (3.5 kDa) was dissolved in a saturated solution of α-CDs (1.01 g in 7 mL of DI water) and stirred for 24 h at room temperature to give linear polypseudorotaxane as white precipitate. The precipitate was collected via centrifugation at 3,000 rcf for 10 min and lyophilized. The lyophilized white powder (190 mg) was then dissolved in a mixture solution of Z-L-tyrosine-OH (82 mg), HOBt (35 mg), BOP (115 mg) and DIEA (45 μL) in 0.5 mL anhydrous DMF. The reaction was stirred at room temperature for 24 h. The mixture was precipitated in 50 mL diethyl ether, and sequentially washed by acetone (50 mL), methanol (50 mL) and DI water (50 mL). The dried precipitate (108 mg) was dissolved in 2 mL dry DMSO and CDI (300 mg) was added. The reaction was stirred for 3 h under nitrogen atmosphere. DMAE (1 mL) was then added dropwise to the solution, and the reaction was further stirred overnight at room temperature. The resulting mixture was precipitated in diethyl ether and washed in succession in acetone (50 mL), methanol (50 mL). The precipitate was redissolved in DI water, dialyzed against DI water for 72 h (MWCO = 3 kDa) and lyophilized to result in linear PRX.

4.4 Physicochemical characterization of plasmid laden 4-arm PRX

The size and ζ-potential of plasmid laden 4-arm PRX were measured by a ZETAPALS instrument (Brookhaven Instruments Corporation), with an equivalent plasmid concentration of 1 μg/mL. The morphology of plasmid laden 4-arm PRX was visualized by atomic force microscope (AFM). Plasmid laden 4-arm PRX was directly added to mica substrate (1 cm ×1 cm), and free plasmid was premixed with 5 mM $MgCl_2$-HEPES buffer before addition to mica substrate. The equivalent concentration of plasmid was 0.2 μg/mL. The samples were dried with nitrogen gas and imaged on Bruker Dimension FastScan AFM. DNA gel retardation assay was performed with Precast agarose gel (Sigma Aldrich). Plasmid DNA was complexed with 4-arm PRX analogues in multiple N/P ratio. Samples were loaded in gel loading buffer (Sigma Aldrich), running in TBE buffer at 150 V for 30 min, followed by visualization on gel imaging system (MultiImage II AlphaImager HP, Alpha Innotech).

4.5 *In vitro* cell culture and transfection

To facilitate bioluminescence imaging of tumor growth, MC38 colon adenocarcinoma cells were permanently transfected with a luciferase-lentiviral vector in the UCLA vector core facility, as previously described [63]. Limiting dilution was performed to generate monoclonal MC38-luc cells. MC38 cells were cultured in DMEM, supplemented with 10% FBS, 100 U/mL penicillin, 100 μg/mL streptomycin, and 2 mM L-glutamine. 24 h prior to transfection, MC38 cells were seeded at 1×10^4 cells/well on 96-well plates. Plasmid encoding tdTomato reporter protein was complexed with 4-arm PRX analogues in multiple N/P ratios and incubated with MC38 cells (1 μg plasmid/mL) in medium containing 10% FBS. MC38 cells were further incubated for 72 h and the expression of tdTomato was examined on a fluorescence microscope (Observer D1, Zeiss). For pIL-12 transfection, optimized 4-arm PRX or linear PRX were complexed with pIL-12 and incubated with MC38 cells (1 μg plasmid/mL) for 72 h. Untreated MC 38 cells or MC38 cells treated with control plasmid (pC) laden 4-arm PRX were also detected as control. The supernatant of cell culture

media were collected and subjected to ELISA detection of IL-12 p70 protein. RT-PCR was also performed to identify the expression of IL-12 (n=6).

4.6 Native gel electrophoresis

Mouse immunoglobulin (IgG) was prepared as 10 μg/μL aqueous solution and incubated with pIL-12 laden optimized 4-arm PRX or linear PRX (plasmid concentration 1 μg/μL) for 30 min at 37 °C. The treated IgG solutions were directly loaded in 4–16% NativePAGE gel system (10 μg IgG per lane) for 100 min at 150 V. The protein bands were visualized by Coomassie blue staining. The intensity of IgG band was semi-quantified by Image J software.

4.7 *In vivo* biodistribution and PK study

Female C57BL/6 mice (~8 weeks) were purchased from The Jackson Laboratory and maintained under pathogen-free conditions. All animal experiments were performed with protocols approved by the UCLA Animal Research Committee. To study the PK profile, Cy3-labeled plasmid was prepared with Label IT® Tracker™ kit (Mirus Bio) according to manufacturer's instruction. Normal C57BL/6 mice received single IV injection of Cy3-labeled plasmid laden 4-arm PRX or linear PRX (5 mg plasmid/kg) (n=3). Plasma was collected at the indicated time points (0.083, 1, 2, 4, 8 and 24 h). The fluorescence intensity of plasma samples were detected on microplate reader (M5e, Molecular Device), with Ex/Em of 544nm/590nm. The plasmid concentration in the sample was calculated based on the fluorescence intensity using the standard curve of plasmid. The PK profiles of Cy3-labeled plasmid were assessed using PKsolver software [26]. We continued to perform biodistribution study in a subcutaneous tumor bearing mice model. Female C57BL/6 mice were subcutaneously inoculated in the right flank with MC38 cells (1×10^6 cells/mouse). The animals were maintained under pathogen-free conditions and all animal experiments were approved by the UCLA Animal Research Committee. Following tumor growth to 8–10 mm in size, mice were IV injected with Cy3-labeled plasmid laden 4-arm PRX, or linear PRX (5 mg plasmid/kg) (n=3). 24 h post IV injection, the mice were sacrificed to collect tumors and the major organs (heart, liver, spleen, lung and kidney). Ex-vivo imaging was performed on IVIS system (Xenogen) with Ex/Em of 535nm/575–650nm. Tumor tissues were then embedded in OCT reagents and cryo-sectioned. CD31 immuno-fluorescence staining was performed to locate the blood vessels as we shown before [64]. The intratumoral distribution of Cy3-labeled plasmid was visualized by confocal microscopy (SP8-SMD, Leica).

4.8 Short-term *in vivo* efficacy study

To study the short-term efficacy, C57/BL6 mice bearing subcutaneous MC38 tumors were IV injected with pIL-12 laden 4-arm PRX (5 mg plasmid/kg), pC laden 4-arm PRX (as non-functional control) or saline (n=4). To validate the *in vivo* transfection efficacy, western blot detection of tdTomato reporter protein was performed in MC38 tumors 7 days post IV injection. The snap-frozen MC38 tumors were weighed and homogenized in RIPA buffer (Cell Signaling Technology) supplemented with protease inhibitor cocktail (Roche Diagnostics), followed by centrifugation at 10,000 rcf for 20 min. Western blot was performed according to published procedures [48]. Briefly, electrophoresis was performed on 4–12% SDS-PAGE gel (Invitrogen), and the proteins were subsequently transferred to a

PVDF membrane. After blocking in 5% BSA, the membrane was overlaid with primary antibodies including anti-mCherry (ab167453, Abcam) to detect tdTomato and anti-vinculin XP® mAb (Cell Signaling Technology) as loading control. Staining with HRP-conjugated secondary antibodies was sequentially performed and the blots were developed by the addition of the ECL solution.

To detect the IL-12 expression *in vivo*, 3 and 7 days post IV injection, the mice were sacrificed, and tumors, major organs (heart, liver, spleen, lung and kidney) were collected and snap-frozen in liquid nitrogen. Serum was also collected for IL-12 detection. For ELISA detection of IL-12, the snap-frozen MC38 tumors and major organs were weighed, cut into pieces and suspended in tissue extraction reagent I (Invitrogen) supplemented with protease inhibitor cocktail (Roche Diagnostics). Tissue samples were then homogenized on ice and centrifuged at 10,000 rcf for 20 min. Serum samples were centrifuged at 3,000 rpm for 10 min before testing. The above procedures were all performed at 4 °C. The IL-12 p70 protein level in tissue extracts and plasma was determined by Quantikine ELISA Kit (R&D Systems).

4.9 *In vivo* antitumor efficacy study

Female C57BL/6 mice were subcutaneously inoculated in the right flank with MC38-luc cells (1×10^6 cells/mouse). Following tumor growth to 5–8 mm in size, C57BL/6 mice were randomly assigned to 3 groups (n=4), and received IV injection of pIL-12 laden 4-arm PRX, pC laden 4-arm PRX as non-functional control, or saline twice per week (5 mg plasmid/kg/injection, 5 injections in total). To monitor the tumor burden weekly, mice received intraperitoneal injection of 75 mg/kg D-Luciferin for 8 min, before IVIS detection of bioluminescent signal from tumor site. Quantitative expression of tumor growth was obtained by normalizing the bioluminescent radiance of tumor to day 1. The size of the tumor were also measured by caliper and plotted vs. time. The size of tumor was calculated as $\pi/6\times\text{length}\times\text{width}^2$, in which a represented width of the rumor and b represented the length of the tumor. The animals were sacrificed on day 21, and the tumor tissues were collected for further analysis.

4.10 Flow cytometry analysis

Right after tissue collection on day 21, the treated MC38 tumors were cut into smaller pieces digested in DMEM with 0.5 mg/mL collagenase type I (Worthington Biochemical Corporation) at 37 °C for 1 h. The digested tissues were gently meshed though a 70 μm cell strainer and treated by ACK lysing buffer (Gibco) as per manufacturer's instructions. The harvested cells were washed twice and resuspended in stain buffer (BD Pharmigen), and incubated with FcBlock (TruStain fcXTM anti-mouse CD16/32, clone 93, BioLegend) to avoid nonspecific binding. Staining was then performed with primary antibodies for 30 min at 4 °C. The following anti-mouse antibodies were purchased from eBiosciences: CD45-eFluor 450 (clone 30-F11), CD8α-Alexa Flour 488 (clone 53–6.7), NK1.1-PerCP-Cyanine 5.5 (clone PK136), CD3e-APC-eFlour780 (clone 17A2). For the staining of intracellular Interferon-γ, the cell were treated with intracellular fixation and permeabilization kit (eBioscience) as per manufacturer's instruction, and stained with anti-Interferon-γ-APC (clone XMG1.2, eBioscience). After washing, cells were analyzed on a flow cytometer

(LSRII, BD Biosciences). The data were processed by FlowJo software (Tree Star). Dead cells and doublets were excluded based on forward and side scatter.

4.11 Immunohistochemistry (IHC) and immunofluorescence staining

MC38 Tumor tissues harvested on day 21 were fixed in 10% formalin solution. Tissue sectioning and IHC staining were performed by the UCLA Jonsson Comprehensive Cancer Center Translational Pathology Core Laboratory. Briefly, the slides were deparaffinized, incubated in 3% methanol-hydrogen peroxide, followed by incubation with 10 mM EDTA at 95 °C using the Decloaking Chamber (Biocare Medical, DC2012). The slides were incubated with individual primary antibodies for 1 h including anti-CD8 (eBioscience, 4SM15, 1/100), anti-NK1.1 (Bioss, bs4682R, 1/100), anti-IFN-γ (Abcam, ab9657, 1/200) or anti-IL-12p70 (Novus Biologics, NBP1–85564, 1/100). After washing, the slides were further incubated with HRP-conjugated secondary antibodies at room temperature for 30 min. After rinsing with PBST, the slides were incubated with 3,3′-diaminobenzidine and counterstained with hematoxylin. The slides were scanned by an Aperio AT Turbo Digital Pathology Scanner (Leica Biosystems).

To determine the density of CD31-positive blood vessels and evaluate the anti-angiogenesis effect, the treated MC38 tumor tissues harvested on day 21 were embedded with OCT reagent and cyro-sectioned. The sections were stained with anti-CD31 monoclonal antibody (Clone 390, BD Pharmingen) at 4 °C overnight. After removal of the primary antibody and washing in PBS 3 times, the Alexa Fluor® 647 secondary antibody was added and incubated for 1 h at room temperature, and counter-stained with DAPI. The stained slides were examined with a confocal microscope (SP8-SMD, Leica).

4.12 Safety profile of pIL-12 laden 4-arm PRX

IV injection of pIL-12 laden 4-arm PRX, pC laden 4-arm PRX as non-functional control or saline was performed in healthy C57BL/6 mice. The dose and injection scheme was the same as the antitumor efficacy study. For comparison, we also included IV mouse rIL-12 at a therapeutic dose (100 μg/kg) [37]. Blood were collected on day 7 and day 21, and blood chemistry test were also performed by Pathology & Laboratory Medicine Services from UCLA Division of Laboratory Animal Medicine (DLAM). Major organs were collected and fixed in 10% formalin, followed by paraffin embedding. Tissue sections were stained by Haemotoxylin and Eosin (H&E) for histological analysis.

4.13 Statistical analysis

Comparative analysis of the differences between groups was performed using one-way ANNOVA followed by Tukey's post hoc test. A statistically significant difference was determined at $p < 0.05$. Values were expressed as mean ± SD of multiple determinations, as stated in the figure legends.

5. Data availability statement

The data are available from the corresponding author on reasonable request.

Supplementary Material

Refer to Web version on PubMed Central for supplementary material.

References:

[1]. Wenz G, Han B-H, Müller A, Cyclodextrin rotaxanes and polyrotaxanes, Chemical Reviews 106(3) (2006) 782–817. [PubMed: 16522009]

[2]. Li J, Yang C, Li H, Wang X, Goh SH, Ding JL, Wang DY, Leong KW, Cationic supramolecules composed of multiple oligoethylenimine-grafted β-cyclodextrins threaded on a polymer chain for efficient gene delivery, Advanced Materials 18(22) (2006) 2969–2974.

[3]. Ooya T, Choi HS, Yamashita A, Yui N, Sugaya Y, Kano A, Maruyama A, Akita H, Ito R, Kogure K, Biocleavable polyrotaxane– plasmid DNA polyplex for enhanced gene delivery, Journal of the American Chemical Society 128(12) (2006) 3852–3853. [PubMed: 16551060]

[4]. Davis ME, The first targeted delivery of siRNA in humans via a self-assembling, cyclodextrin polymer-based nanoparticle: from concept to clinic, Molecular pharmaceutics 6(3) (2009) 659–668. [PubMed: 19267452]

[5]. Mellet CO, Fernández JMG, Benito JM, Cyclodextrin-based gene delivery systems, Chemical Society Reviews 40(3) (2011) 1586–1608. [PubMed: 21042619]

[6]. Li J, Loh XJ, Cyclodextrin-based supramolecular architectures: syntheses, structures, and applications for drug and gene delivery, Advanced drug delivery reviews 60(9) (2008) 1000–1017. [PubMed: 18413280]

[7]. Yamashita A, Yui N, Ooya T, Kano A, Maruyama A, Akita H, Kogure K, Harashima H, Synthesis of a biocleavable polyrotaxane-plasmid DNA (pDNA) polyplex and its use for the rapid nonviral delivery of pDNA to cell nuclei, Nature protocols 1(6) (2006) 2861. [PubMed: 17406545]

[8]. Badwaik VD, Aicart E, Mondjinou YA, Johnson MA, Bowman VD, Thompson DH, Structure-property relationship for in vitro siRNA delivery performance of cationic 2-hydroxypropyl-β-cyclodextrin: PEG-PPG-PEG polyrotaxane vectors, Biomaterials 84 (2016) 86–98. [PubMed: 26826298]

[9]. Tamura A, Yui N, Cellular internalization and gene silencing of siRNA polyplexes by cytocleavable cationic polyrotaxanes with tailored rigid backbones, Biomaterials 34(10) (2013) 2480–2491. [PubMed: 23332177]

[10]. Kayashima H, Toshima T, Okano S, Taketomi A, Harada N, Yamashita Y.-i., Tomita Y, Shirabe K, Maehara Y, Intratumoral neoadjuvant immunotherapy using IL-12 and dendritic cells is an effective strategy to control recurrence of murine hepatocellular carcinoma in immunosuppressed mice, The Journal of Immunology 185(1) (2010) 698–708. [PubMed: 20498356]

[11]. Morille M, Passirani C, Vonarbourg A, Clavreul A, Benoit J-P, Progress in developing cationic vectors for non-viral systemic gene therapy against cancer, Biomaterials 29(24–25) (2008) 3477–3496. [PubMed: 18499247]

[12]. Suk JS, Xu Q, Kim N, Hanes J, Ensign LM, PEGylation as a strategy for improving nanoparticle-based drug and gene delivery, Advanced drug delivery reviews 99 (2016) 28–51. [PubMed: 26456916]

[13]. Tugues S, Burkhard S, Ohs I, Vrohlings M, Nussbaum K, Vom Berg J, Kulig P, Becher B, New insights into IL-12-mediated tumor suppression, Cell death and differentiation 22(2) (2015) 237. [PubMed: 25190142]

[14]. Colombo MP, Trinchieri G, Interleukin-12 in anti-tumor immunity and immunotherapy, Cytokine & growth factor reviews 13(2) (2002) 155–168. [PubMed: 11900991]

[15]. Sangro B, Mazzolini G, Ruiz J, Herraiz M, Quiroga J, Herrero I, Benito A, Larrache J, Pueyo J, Subtil JC, Phase I trial of intratumoral injection of an adenovirus encoding interleukin-12 for advanced digestive tumors, Journal of clinical oncology 22(8) (2004) 1389–1397. [PubMed: 15084613]

[16]. Rakhmilevich AL, Turner J, Ford MJ, McCabe D, Sun WH, Sondel PM, Grota K, Yang N-S, Gene gun-mediated skin transfection with interleukin 12 gene results in regression of established

primary and metastatic murine tumors, Proceedings of the National Academy of Sciences 93(13) (1996) 6291–6296.

[17]. Daud AI, DeConti RC, Andrews S, Urbas P, Riker AI, Sondak VK, Munster PN, Sullivan DM, Ugen KE, Messina JL, Phase I trial of interleukin-12 plasmid electroporation in patients with metastatic melanoma, Journal of clinical oncology 26(36) (2008) 5896. [PubMed: 19029422]

[18]. Dass C, Hallaj-Nezhadi S, Lotfipour F, Nanoparticle-mediated interleukin-12 cancer gene therapy, Journal of Pharmacy & Pharmaceutical Sciences 13(3) (2010) 472–485. [PubMed: 21092717]

[19]. Edwards RP, Interleukin-12 in Treating Patients With Refractory Advanced-Stage Ovarian Cancer or Abdominal Cancer, ClinicalTrials.gov Identifier: NCT00003439 (2004).

[20]. Ogris M, Brunner S, Schüller S, Kircheis R, Wagner E, PEGylated DNA/transferrin–PEI complexes: reduced interaction with blood components, extended circulation in blood and potential for systemic gene delivery, Gene therapy 6(4) (1999) 595. [PubMed: 10476219]

[21]. Reineke TM, Davis ME, Structural effects of carbohydrate-containing polycations on gene delivery. 2. Charge center type, Bioconjugate chemistry 14(1) (2003) 255–261. [PubMed: 12526716]

[22]. Pack DW, Hoffman AS, Pun S, Stayton PS, Design and development of polymers for gene delivery, Nature reviews Drug discovery 4(7) (2005) 581. [PubMed: 16052241]

[23]. Mishra S, Webster P, Davis ME, PEGylation significantly affects cellular uptake and intracellular trafficking of non-viral gene delivery particles, European journal of cell biology 83(3) (2004) 97–111. [PubMed: 15202568]

[24]. Ward CM, Read ML, Seymour LW, Systemic circulation of poly (L-lysine)/DNA vectors is influenced by polycation molecular weight and type of DNA: differential circulation in mice and rats and the implications for human gene therapy, Blood 97(8) (2001) 2221–2229. [PubMed: 11290582]

[25]. Fischer D, Bieber T, Li Y, Elsässer H-P, Kissel T, A novel non-viral vector for DNA delivery based on low molecular weight, branched polyethylenimine: effect of molecular weight on transfection efficiency and cytotoxicity, Pharmaceutical research 16(8) (1999) 1273–1279. [PubMed: 10468031]

[26]. Zhang Y, Huo M, Zhou J, Xie S, PKSolver: An add-in program for pharmacokinetic and pharmacodynamic data analysis in Microsoft Excel, Computer methods and programs in biomedicine 99(3) (2010) 306–314. [PubMed: 20176408]

[27]. Aggarwal P, Hall JB, McLeland CB, Dobrovolskaia MA, McNeil SE, Nanoparticle interaction with plasma proteins as it relates to particle biodistribution, biocompatibility and therapeutic efficacy, Advanced drug delivery reviews 61(6) (2009) 428–437. [PubMed: 19376175]

[28]. Owens III DE, Peppas NA, Opsonization, biodistribution, and pharmacokinetics of polymeric nanoparticles, International journal of pharmaceutics 307(1) (2006) 93–102. [PubMed: 16303268]

[29]. Maeda H, Wu J, Sawa T, Matsumura Y, Hori K, Tumor vascular permeability and the EPR effect in macromolecular therapeutics: a review, Journal of controlled release 65(1–2) (2000) 271–284. [PubMed: 10699287]

[30]. Moghimi SM, Hunter AC, Murray JC, Long-circulating and target-specific nanoparticles: theory to practice, Pharmacological reviews 53(2) (2001) 283–318. [PubMed: 11356986]

[31]. Meng H, Mai WX, Zhang H, Xue M, Xia T, Lin S, Wang X, Zhao Y, Ji Z, Zink JI, Codelivery of an optimal drug/siRNA combination using mesoporous silica nanoparticles to overcome drug resistance in breast cancer in vitro and in vivo, ACS nano 7(2) (2013) 994–1005. [PubMed: 23289892]

[32]. Meng H, Zhao Y, Dong J, Xue M, Lin Y-S, Ji Z, Mai WX, Zhang H, Chang CH, Brinker CJ, Two-wave nanotherapy to target the stroma and optimize gemcitabine delivery to a human pancreatic cancer model in mice, ACS nano 7(11) (2013) 10048–10065. [PubMed: 24143858]

[33]. Kano MR, Bae Y, Iwata C, Morishita Y, Yashiro M, Oka M, Fujii T, Komuro A, Kiyono K, Kaminishi M, Improvement of cancer-targeting therapy, using nanocarriers for intractable solid tumors by inhibition of TGF-β signaling, Proceedings of the National Academy of Sciences 104(9) (2007) 3460–3465.

[34]. Liu X, Lin P, Perrett I, Lin J, Liao Y-P, Chang CH, Jiang J, Wu N, Donahue T, Wainberg Z, Nel AE, Meng H, Tumor-penetrating peptide enhances transcytosis of silicasome-based chemotherapy for pancreatic cancer, The Journal of Clinical Investigation 127(5) (2017) 2007–2018. [PubMed: 28414297]

[35]. Lasek W, Zagożdżon R, Jakobisiak M, Interleukin 12: still a promising candidate for tumor immunotherapy?, Cancer Immunology, Immunotherapy 63(5) (2014) 419–435. [PubMed: 24514955]

[36]. Melero I, Duarte M, Ruiz J, Sangro B, Galofré JC, Mazzolini G, Bustos M, Qian C, Prieto J, Intratumoral injection of bone-marrow derived dendritic cells engineered to produce interleukin-12 induces complete regression of established murine transplantable colon adenocarcinomas, Gene therapy 6(10) (1999) 1779. [PubMed: 10516729]

[37]. Brunda MJ, Luistro L, Warrier RR, Wright RB, Hubbard BR, Murphy M, Wolf SF, Gately M, Antitumor and antimetastatic activity of interleukin 12 against murine tumors, Journal of Experimental Medicine 178(4) (1993) 1223–1230. [PubMed: 8104230]

[38]. Cui J, Shin T, Kawano T, Sato H, Kondo E, Toura I, Kaneko Y, Koseki H, Kanno M, Taniguchi M, Requirement for Vα14 NKT cells in IL-12-mediated rejection of tumors, Science 278(5343) (1997) 1623–1626. [PubMed: 9374462]

[39]. Tahara H, Zeh HJ, Storkus WJ, Pappo I, Watkins SC, Gubler U, Wolf SF, Robbins PD, Lotze MT, Fibroblasts genetically engineered to secrete interleukin 12 can suppress tumor growth and induce antitumor immunity to a murine melanoma in vivo, Cancer research 54(1) (1994) 182–189. [PubMed: 7903204]

[40]. Car BD, Eng VM, Lipman JM, Anderson TD, The toxicology of interleukin-12: a review, Toxicologic pathology 27(1) (1999) 58–63. [PubMed: 10367675]

[41]. Lenzi R, Interleukin-12 in Treating Patients With Cancer in the Abdomen, ClinicalTrials.gov Identifier: NCT00003046, (2004) (2004).

[42]. Carson W, Cetuximab and Recombinant Interleukin-12 in Treating Patients With Squamous Cell Carcinoma of the Head and Neck That is Recurrent, Metastatic, or Cannot Be Removed by Surgery, ClinicalTrials.gov Identifier: NCT01468896, (2011).

[43]. Ryffel B, Interleukin-12: role of interferon-γ in IL-12 adverse effects, Clinical immunology and immunopathology 83(1) (1997) 18–20. [PubMed: 9073529]

[44]. Dow SW, Fradkin LG, Liggitt DH, Willson AP, Heath TD, Potter TA, Lipid-DNA complexes induce potent activation of innate immune responses and antitumor activity when administered intravenously, The Journal of Immunology 163(3) (1999) 1552–1561. [PubMed: 10415059]

[45]. Lohr F, Lo DY, Zaharoff DA, Hu K, Zhang X, Li Y, Zhao Y, Dewhirst MW, Yuan F, Li C-Y, Effective tumor therapy with plasmid-encoded cytokines combined with in vivo electroporation, Cancer research 61(8) (2001) 3281–3284. [PubMed: 11309280]

[46]. Caruso M, Pham-Nguyen K, Kwong Y-L, Xu B, Kosai K-I, Finegold M, Woo S, Chen S-H, Adenovirus-mediated interleukin-12 gene therapy for metastatic colon carcinoma, Proceedings of the National Academy of Sciences 93(21) (1996) 11302–11306.

[47]. Mazzolini G, Qian C, Xie X, Sun Y, Lasarte JJ, Drozdzik M, Prieto J, Regression of colon cancer and induction of antitumor immunity by intratumoral injection of adenovirus expressing interleukin-12, Cancer gene therapy 6(6) (1999) 514. [PubMed: 10608348]

[48]. Lu J, Liu X, Liao Y-P, Salazar F, Sun B, Jiang W, Chang CH, Jiang J, Wang X, Wu AM, Nano-enabled pancreas cancer immunotherapy using immunogenic cell death and reversing immunosuppression, Nature communications 8(1) (2017) 1811.

[49]. Leonard JP, Sherman ML, Fisher GL, Buchanan LJ, Larsen G, Atkins MB, Sosman JA, Dutcher JP, Vogelzang NJ, Ryan JL, Effects of single-dose interleukin-12 exposure on interleukin-12–associated toxicity and interferon-γ production, Blood 90(7) (1997) 2541–2548. [PubMed: 9326219]

[50]. Fallon J, Tighe R, Kradjian G, Guzman W, Bernhardt A, Neuteboom B, Lan Y, Sabzevari H, Schlom J, Greiner JW, The immunocytokine NHS-IL12 as a potential cancer therapeutic, Oncotarget 5(7) (2014) 1869. [PubMed: 24681847]

[51]. Hernandez-Alcoceba R, Poutou J, Ballesteros-Briones MC, Smerdou C, Gene therapy approaches against cancer using in vivo and ex vivo gene transfer of interleukin-12, Immunotherapy 8(2) (2016) 179–198. [PubMed: 26786809]

[52]. Thaker PH, Brady WE, Lankes HA, Odunsi K, Bradley WH, Moore KN, Muller CY, Anwer K, Schilder RJ, Alvarez RD, A phase I trial of intraperitoneal GEN-1, an IL-12 plasmid formulated with PEG-PEI-cholesterol lipopolymer, administered with pegylated liposomal doxorubicin in patients with recurrent or persistent epithelial ovarian, fallopian tube or primary peritoneal cancers: An NRG Oncology/Gynecologic Oncology Group study, Gynecologic oncology 147(2) (2017) 283–290. [PubMed: 28802766]

[53]. Lengyel E, Ovarian Cancer Development and Metastasis, The American Journal of Pathology 177(3) (2010) 1053–1064. [PubMed: 20651229]

[54]. Sadahiro S, Suzuki T, Tanaka A, Okada K, Kamata H, Hematogenous Metastatic Patterns of Curatively Resected Colon Cancer Were Different from Those of Stage IV and Autopsy Cases, Japanese Journal of Clinical Oncology 43(4) (2013) 444–447. [PubMed: 23365110]

[55]. Leake I, Understanding the routes of metastasis in colorectal cancer, Nature Reviews Gastroenterology &Amp; Hepatology 11 (2014) 270.

[56]. Hallaj-Nezhadi S, Lotfipour F, D. C., Nanoparticle-mediated interleukin-12 cancer gene therapy, J Pharm Pharm Sci 13 (2010) 472–485. [PubMed: 21092717]

[57]. Lasek W, Zagozdzon R, Clinical trials with IL-12 in cancer immunotherapy, Interleukin 12: Antitumor Activity and Immunotherapeutic Potential in Oncology, Springer2016, pp. 43–75.

[58]. Addison C, Bramson J, Hitt M, Muller W, Gauldie J, Graham F, Intratumoral coinjection of adenoviral vectors expressing IL-2 and IL-12 results in enhanced frequency of regression of injected and untreated distal tumors, Gene therapy 5(10) (1998) 1400. [PubMed: 9930346]

[59]. Fallon JK, Vandeveer AJ, Schlom J, Greiner JW, Enhanced antitumor effects by combining an IL-12/anti-DNA fusion protein with avelumab, an anti-PD-L1 antibody, Oncotarget 8(13) (2017) 20558. [PubMed: 28423552]

[60]. Zhang J, Zhang L.e., Li S, Yin C, Li C, Wu W, Jiang X, Modification of α-cyclodextrin polyrotaxanes by ATRP for conjugating drug and prolonging blood circulation, ACS Biomaterials Science & Engineering 4(6) (2017) 1963–1968.

[61]. Zhou Y, Wang H, Wang C, Li Y, Lu W, Chen S, Luo J, Jiang Y, Chen J, Receptor-mediated, tumor-targeted gene delivery using folate-terminated polyrotaxanes, Molecular pharmaceutics 9(5) (2012) 1067–1076. [PubMed: 22482910]

[62]. Yu G, Yang Z, Fu X, Yung BC, Yang J, Mao Z, Shao L, Hua B, Liu Y, Zhang F, Polyrotaxane-based supramolecular theranostics, Nature communications 9(1) (2018) 766.

[63]. Meng H, Wang M, Liu H, Liu X, Situ A, Wu B, Ji Z, Chang CH, Nel AE, Use of a Lipid-Coated Mesoporous Silica Nanoparticle Platform for Synergistic Gemcitabine and Paclitaxel Delivery to Human Pancreatic Cancer in Mice, ACS Nano 9(4) (2015) 3540–3557. [PubMed: 25776964]

[64]. Meng H, Xue M, Xia T, Ji Z, Tarn DY, Zink JI, Nel AE, Use of size and a copolymer design feature to improve the biodistribution and the enhanced permeability and retention effect of doxorubicin-loaded mesoporous silica nanoparticles in a murine xenograft tumor model, ACS nano 5(5) (2011) 4131–4144. [PubMed: 21524062]

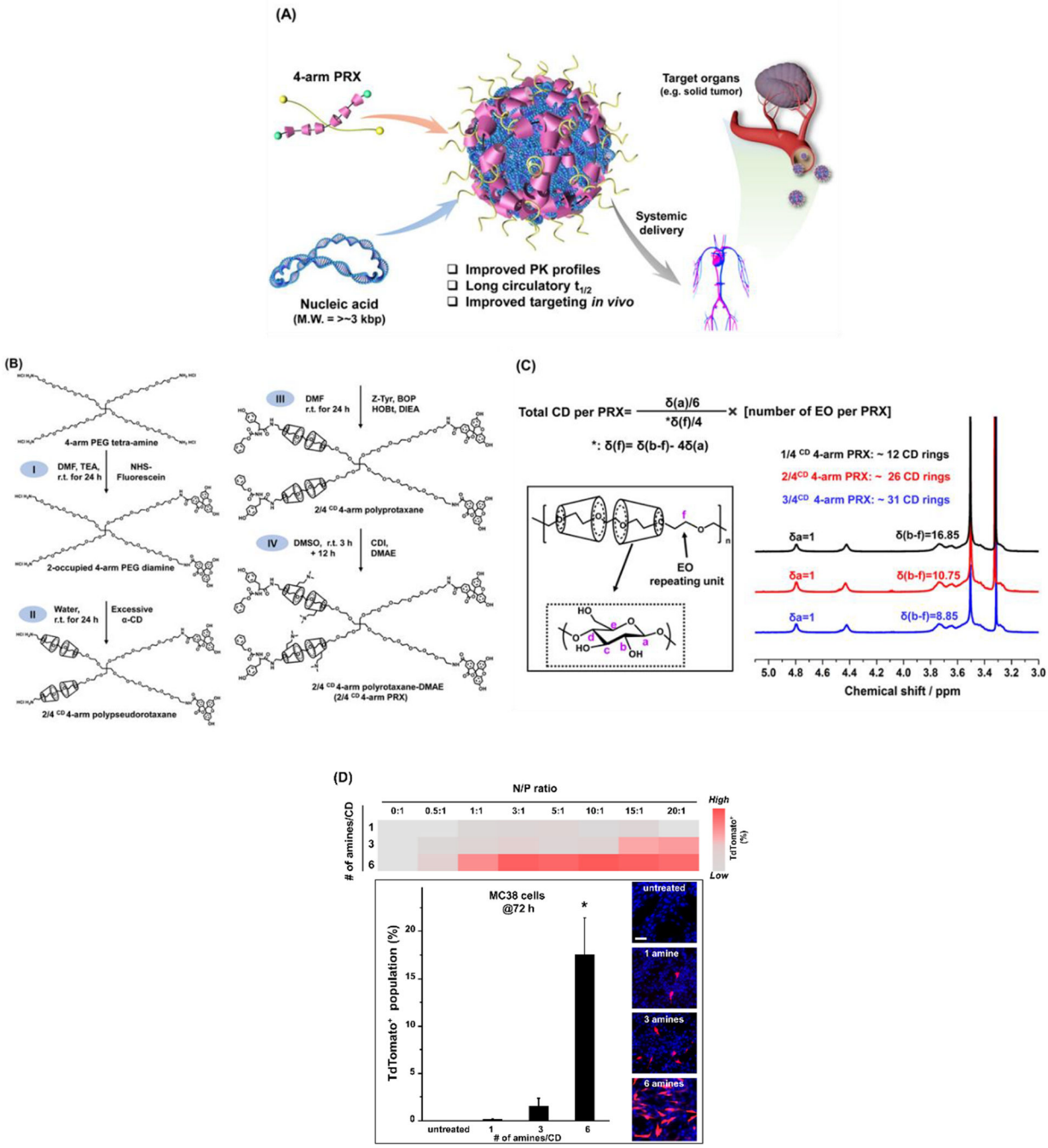

Figure 1.

(A) Schematic of 4-arm PRX platform for systemic plasmid delivery. Cationic α-CDs were threaded onto 4-arm PEG backbone in a spatially selective fashion, resulting in available PEG moieties for enhanced delivery performances *in vivo*. (B) The synthesis routes of 4-arm PRX. Detailed synthetic procedures were described in the result and method sections. (C) Optimizing the cationic charge density on α-CD rings. From the ^{1}H-NMR spectra, the amine density was determined by dividing the relative molar number of $-N(CH_3)_2$ (integration δg divided by 6 protons) with the relative molar number of α-CDs (integration

δa divided by 6 glucose units). (D) *In vitro* transfection of tdTomato reporter plasmid by 4-arm PRX with different charge densities. 4-arm PRXs with ~1, ~3 or ~6 amines per α-CD were complexed with tdTomato plasmid at multiple N/P ratios and incubated with MC38 colon cancer cells for 72 h (1 μg plasmid/mL). The incubation time was determined by a pilot experiment demonstrating a plateau tdTomato expression at 72 h in MC38 cells. The percentages of $tdTomato^+$ MC38 cells were quantitatively displayed at various N/P ratios in the heat map. *In vitro* transfection efficiency at the optimum N/P ratio was compared between 4-arm PRX with different charge densities. Representative fluorescence image of $tdTomato^+$ MC38 cells (red) confirmed that 4-arm PRX with 6 amines per α-CD resulted in the most efficient reporter transfection *in vitro*. Nuclei were counterstained with DAPI. Scale bar represents 50 μm. The results are expressed as mean ± SD (n=6). $*p < 0.05$.

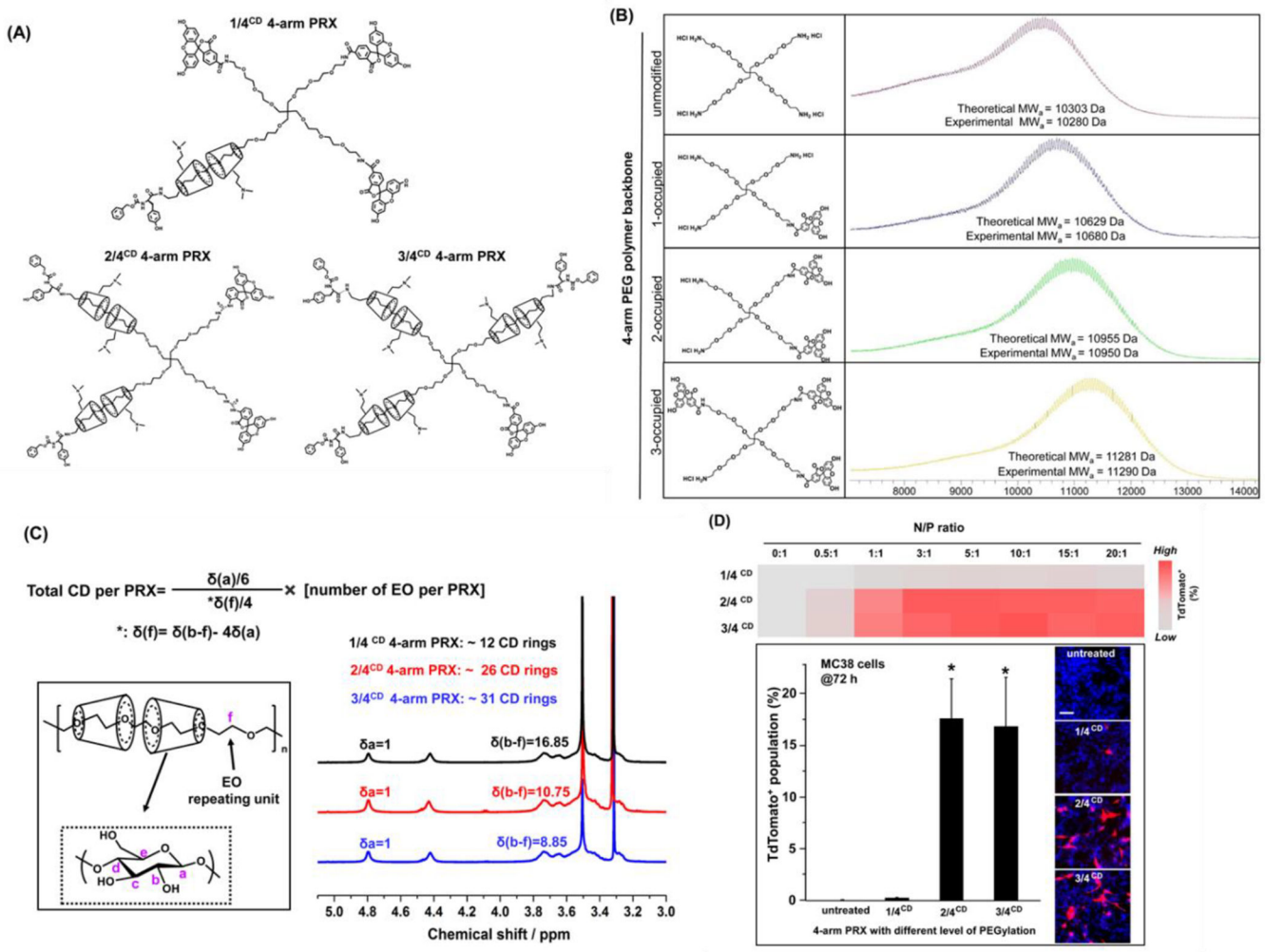

Figure 2.

Use of abiotic and *in vitro* assays to optimize the α-CD numbers and degree of free PEG arms. (A) The chemical structure of 4-arm PRX with different level of available PEG moieties, which was achieved by selectively introducing the bulky end-caps to prevent α-CD threading. (B) The structural scheme of 4-arm PEG precursors selectively occupied with different number of end-caps. MALDI-TOF molecular weight detection demonstrated the synthesis success of the 4-arm PEG precursors. (C) 4-arm PRX with different level of PEGylation was resulted from the aforementioned precursors, which were further confirmed by the α-CD numbers determined from ^{1}H-NMR spectra. The molar ratio between α-CD and EO repeating units in 4-arm PEG backbone was calculated by dividing the relative molar number of α-CD (integration δa divided by 6 glucose units from α-CD) with the relative molar number of EO units (integration δf divided by 4 protons). The ratio is multiplied by the actual molar number of EO per PRX (227 for 10kDa backbone), to give the total number of α-CD per PRX. (D) *In vitro* reporter gene transfection efficiency of 1/4^{CD}, 2/4^{CD}, and 3/4^{CD} 4-arm PRX analogues were compared in terms of heat map display and the representative tdTomato expression at optimum N/P ratio. Scale bar represents 50 μm. The results are expressed as mean ± SD (n=6). *$p < 0.05$.

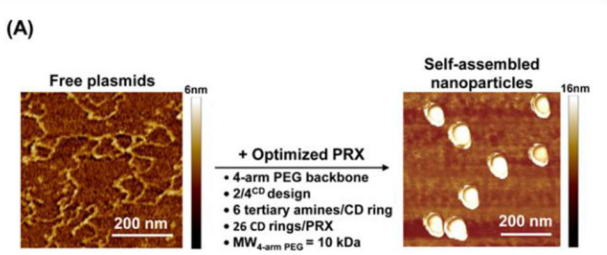

Physicochemical properties of PRX/plasmid nanoparticles

Primary size (AFM)	~ 109 ± 11.4 nm
Hydrodynamic size (DLS) in H_2O	~172 ± 8.7 nm (PDI = 0.18)
Hydrodynamic size (DLS) in DMEM with 10% FBS	~193 ± 6.2 nm (PDI = 0.17)
Zeta potential in H_2O	+ 15.3 ± 3.2 mV
Zeta potential in DMEM with 10% FBS	-3.95 ± 1.9 mV
Optimized N/P ratio	3:1
Endotoxin level/Sterility	< 0.5 EU/mL ; sterile

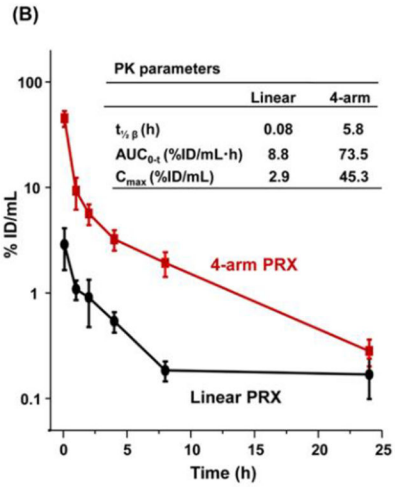

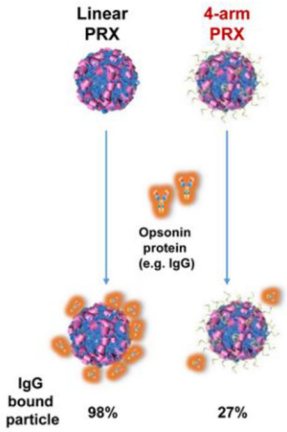

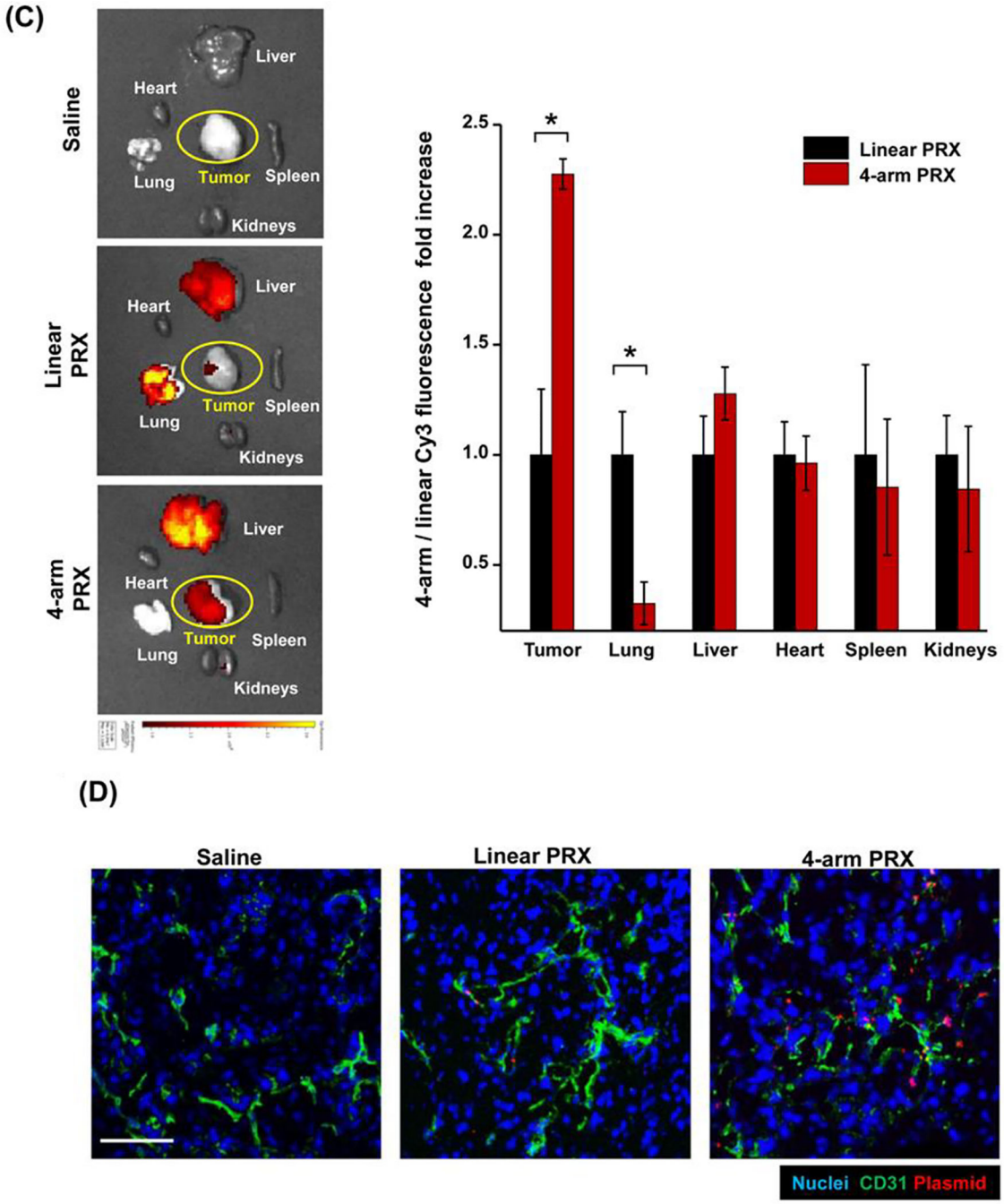

Figure 3.

Optimized 4-arm PRX enhanced the PK and tumor biodistribution of Cy3-labeled plasmid after IV injection in mice. (A) The summary of physicochemical properties of the optimized 4-arm PRX. Representative AFM images of free interleukin-12 plasmid (upper left) and plasmid after complexation with optimized 4-arm PRX (upper right). Scale bar represents 200 nm. (B) Evaluating the PK profile of Cy3-plasmid in C57BL/6 mice. Animals received single IV injection of Cy3-plasmid delivered by optimized 4-arm PRX or linear PRX (5 mg plasmid/kg). Plasma was collected after 0.083, 1, 2, 4, 8 and 24 h. The Cy3-plasmid content

were quantified by fluorescence spectroscopy and expressed as % total injected dose (% ID) per mL. The PK parameters were calculated by PKSolver software. The enhanced circulatory profile of 4-arm PRX were corroborated by significantly reduced binding of IgG (a representative opsonin), which was demonstrated as 27% IgG bound with 4-PRX vs. 98% bound with linear PRX in native gel electrophoresis. (C) In a separate study, MC38 subcutaneous tumor bearing mice received single IV injection of Cy3-pIL-12 delivered by 4-arm PRX or linear PRX (5 mg plasmid/kg). 24 h post IV injection, tumors and organs were collected for *ex vivo* IVIS imaging. The fold increase of Cy3-pIL-12 in different organs including tumors were compared between 4-arm PRX and linear PRX. (D) Confocal microscopy confirmed higher intratumoral abundance of Cy3-pIL-12 (red) delivered by 4-arm PRX, compared to linear PRX. The blood vessels (green) and nuclei (blue) at the tumor site were stained with anti-CD31 antibody and DAPI, respectively. Scale bar represents 100 μm. The results are expressed as mean ± SD (n=3). $*p < 0.05$.

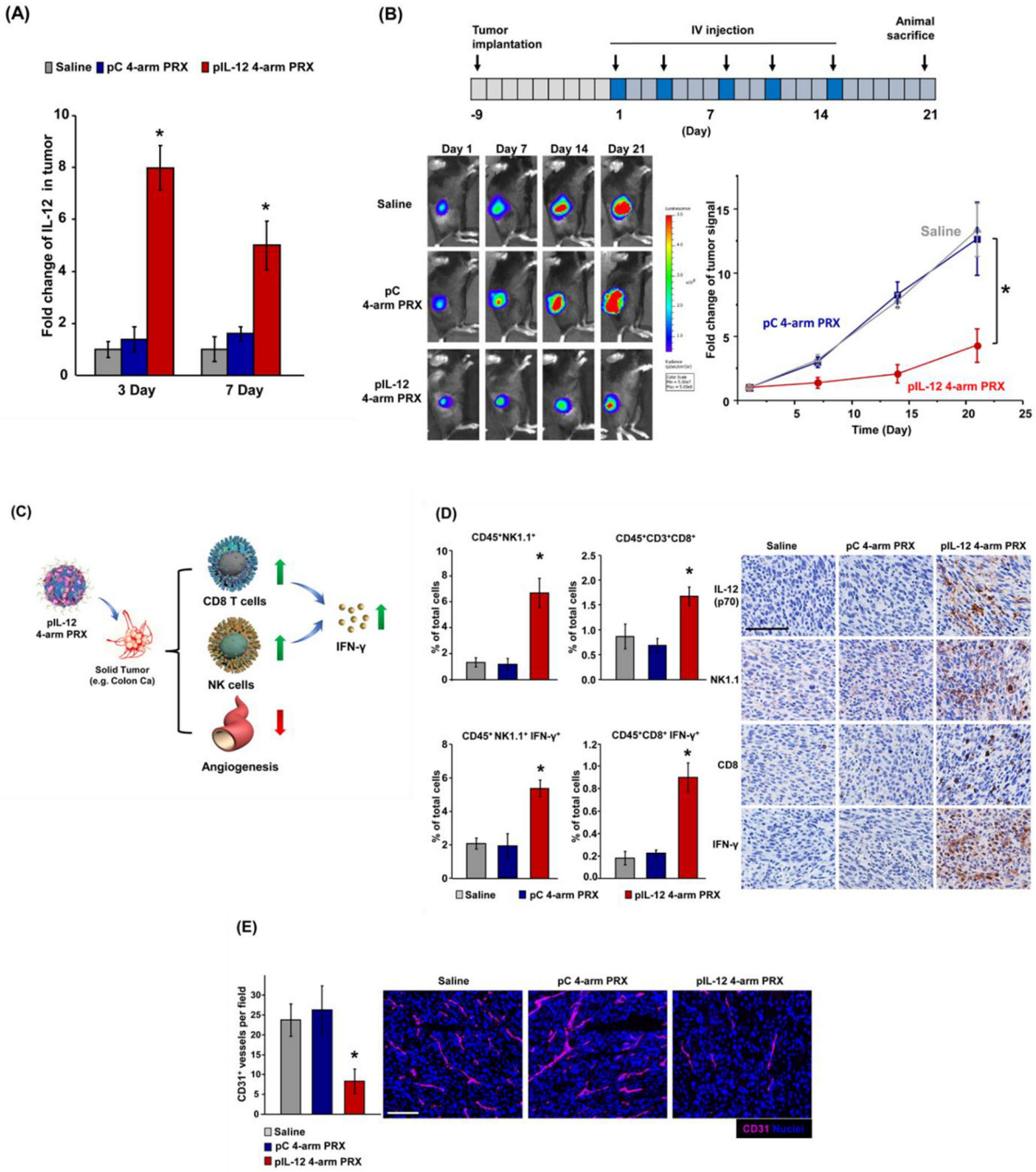

Figure 4.

Systemic delivery of pIL-12 by 4-arm PRX nanocarrier induced effective anti-colon cancer immunity in the MC38-luc tumor model. (A) To demonstrate the time-dependent tumor IL-12 level, MC38-luc tumor bearing mice received single IV injection of pIL-12 laden 4-arm PRX (5 mg plasmid/kg). ELISA detection of IL-12 protein in tumor extracts were performed 3 and 7 day post IV injection. Mice injected with nonfunctional control tdTomato plasmid (pC) laden 4-arm PRX were also tested. (B) In the efficacy study, MC38-luc bearing mice received repetitive IV injection of pIL-12 laden 4-arm PRX (5 mg plasmid/kg/

injection). Interval IVIS imaging was used for monitoring tumor growth, which was quantitatively expressed according to the tumor signal at the operator-defined ROI. Representative bioluminescence images demonstrated the anti-tumor efficacy of pIL-12 laden 4-arm PRX. (C) The scheme for IL-12 mediated anti-tumor immunity, by activation of NK cells, CD8 T cells and anti-angiogenesis machinery in the tumor microenvironment. (D) MC38-luc bearing mice from the same experiment in (B) were sacrificed at day 21. The tumor cells were analyzed by multi-parameter flow cytometry to identify $CD45^+NK1.1^+$ and $CD45^+CD3^+CD8^+$ tumor infiltrating lymphocytes (TILs). IFN-γ secreting TIL population ($IFN\text{-}\gamma^+CD45^+NK1.1^+$ and $IFN\text{-}\gamma^+CD45^+CD8^+$) were also determined. Representative IHC staining of IL-12, NK1.1, CD8 and IFN-γ in tumor section further demonstrated the concurrent innate and adaptive immuno-activation effect of pIL-12 4-arm PRX at the tumor site. (E) Immunofluorescence staining of CD31 (magenta) and quantitative display of $CD31^+$ blood vessel in tumor section confirmed the anti-angiogenesis effect of pIL-12 4-arm PRX. Scale bar represents 100 μm. The results are expressed as mean ± SD (n=4). $*p < 0.05$.

(A)

	7 Day			21 Day			7 Day	21 Day
	Saline	pC 4-arm PRX	pIL-12 4-arm PRX	Saline	pC 4-arm PRX	pIL-12 4-arm PRX	rIL-12	rIL-12
ALT (U/L)	12.5 ± 2.3	16 ± 1.7	23.3 ± 2.4	20.4 ± 3.1	19.2 ± 2.8	21.7 ± 3.5	48.0 ± 3.8*	30.8 ± 6.3*
AST (U/L)	76.2 ± 13.5	83.0 ± 21.2	85.7 ± 14.5	87.7 ± 17.1	98.3 ± 16.0	90.8 ± 18.7	102.5 ± 7.9 *	204.1 ± 30.8*
ALP (U/L)	72.9 ± 7.6	80.3 ± 11.6	84.3 ± 10.1	67.5 ± 9.2	79.5 ± 6.0	83.5 ± 9.1	129.3 ± 15.2*	112.4 ± 9.2*
BUN (mg/dL)	18.3 ± 1.9	19.6 ± 1.4	17.7 ± 2.1	21.7 ± 2.5	24.2 ± 3.3	19.0 ± 1.6	39.4 ± 5.3*	28.4 ± 4.3*
CREAT (mg/dL)	0.27 ± 0.02	0.33 ± 0.03	0.32 ± 0.05	0.30 ± 0.04	0.32 ± 0.05	0.34 ± 0.03	0.47 ± 0.03*	0.40 ± 0.02
RBC (10^3/μL)	9.14 ± 0.61	8.82 ± 0.38	8.98 ± 0.57	8.21 ± 0.44	9.02 ± 0.72	8.61 ± 0.41	7.73 ± 0.87*	7.92 ± 0.77*
PLT (10^3/μL)	819.8 ± 90.4	764.0 ± 134.9	776.1 ± 115.9	843.6 ± 167.5	813.4 ± 75.8	811.2 ± 93.1	735.0 ± 69.2	604.0 ± 59.1*
WBC (10^3/μL)	4.14 ± 0.36	3.82 ± 0.28	1.98 ± 0.17*	3.91 ± 0.24	3.74 ± 0.12	3.67 ± 0.41	1.03 ± 0.05*	4.07 ± 0.55
NE (10^3/μL)	1.20 ± 0.21	1.37 ± 0.08	0.73 ± 0.17*	0.91 ± 0.15	1.02 ± 0.09	1.23 ± 0.21	0.56 ± 0.13*	1.15 ± 0.17
LY (10^3/μL)	2.72 ± 0.61	3.3 ± 0.58	0.98 ± 0.27*	3.2 ± 0.45	3.02 ± 0.49	2.61 ± 0.41	1.63 ± 0.32*	1.82 ± 0.11*
MO (10^3/μL)	0.34 ± 0.12	0.43 ± 0.08	0.26 ± 0.07	0.32 ± 0.05	0.37 ± 0.09	0.44 ± 0.14	0.27 ± 0.03	0.23 ± 0.04

(B)

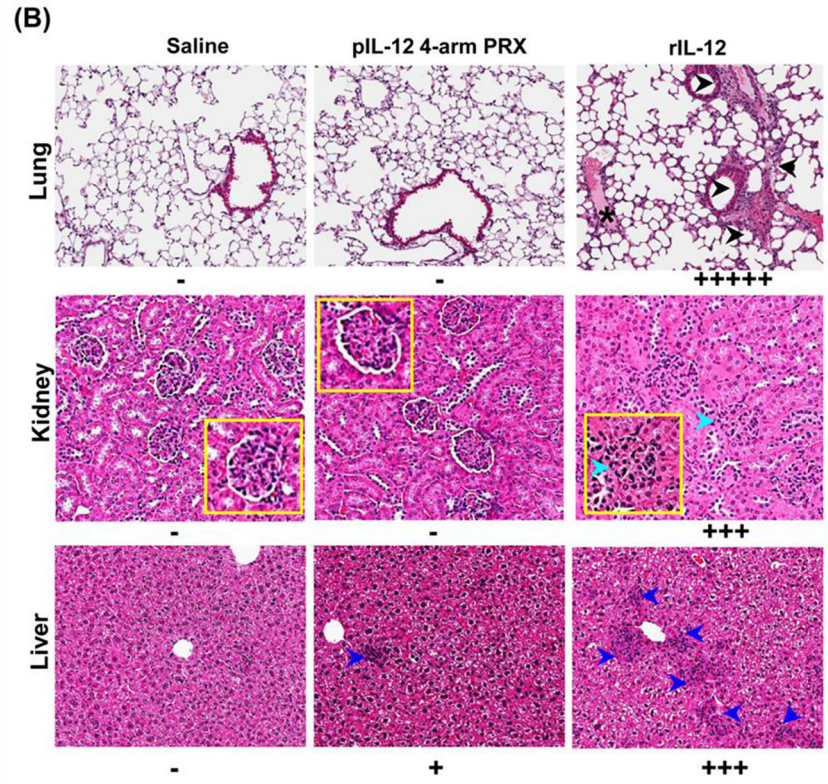

Figure 5.

Multi-arm PRX improved the safety of pIL-12 immunogene therapy. In a separate experiment, healthy C57BL/6 mice received IV injection of pIL-12 laden 4-arm PRX, following the same treatment regimen as the tumor inhibition study shown in Figure 4B. IV injection of saline, pC laden 4-arm PRX and mouse rIL-12 were included as control (n=4). The dose of rIL-12 (100 μg/kg/injection) was designed based on literature.[33] (A) Blood chemistry and complete blood count test were performed on day 7 and day 21. The results are expressed as mean ± SD (n=4). *$p < 0.05$. (B) Representative lung, kidney and liver

histology on day 21. The arrows in the H&E staining of rIL-12 treated lung sections point to interstitial thickening and macrophage infiltrates, and the sites marked with asterisks denote pulmonary edema. The arrows in rIL-12 treated kidneys sections marked the zoomed-in morphology of glomerulus, where glomerular swelling and edema of Bowman's space were observed. While animals treated with rIL-12 showed extensive liver damage, evidenced by large number of infiltrated mononuclear cells, this trend was largely reduced in PRX-treated animals. The degree of damage was ranked using the number of "+". Scale bar represents 200 μm.

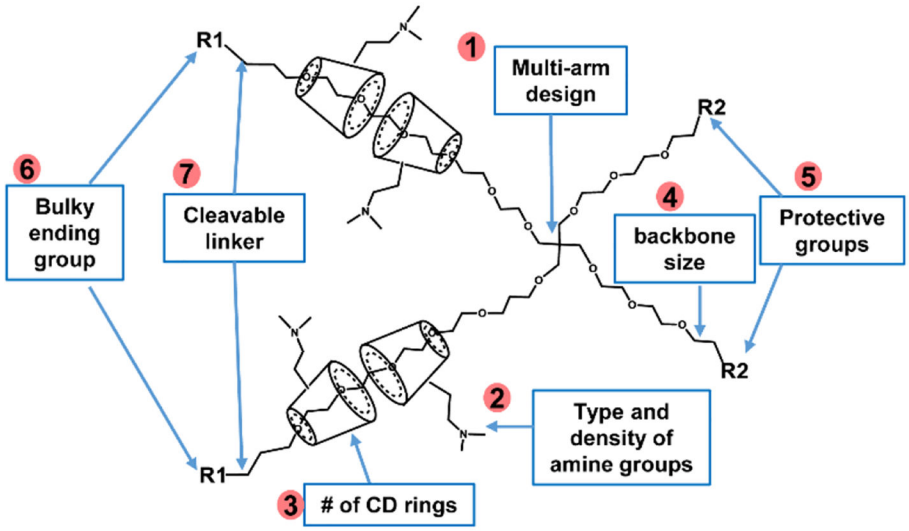

Design	Role
#1	Improve PK and biodistribution
#2	Loading; Transfection efficiency ; Intracellular release; lysosomal escape
#3	Plasmid loading capacity and release
#4	Plasmid loading capacity, particle size
#5	Degree of PEGylation, targeting
#6	Labeling and plasmid release
#7	Intracellular plasmid release

Scheme 1.

Summary of structural design features of multi-arm PRX and their impacts on plasmid delivery.